Cell Reports

Report

Diversity in homeostatic calcium set points predicts retinal ganglion cell survival following optic nerve injury *in vivo*

Graphical abstract

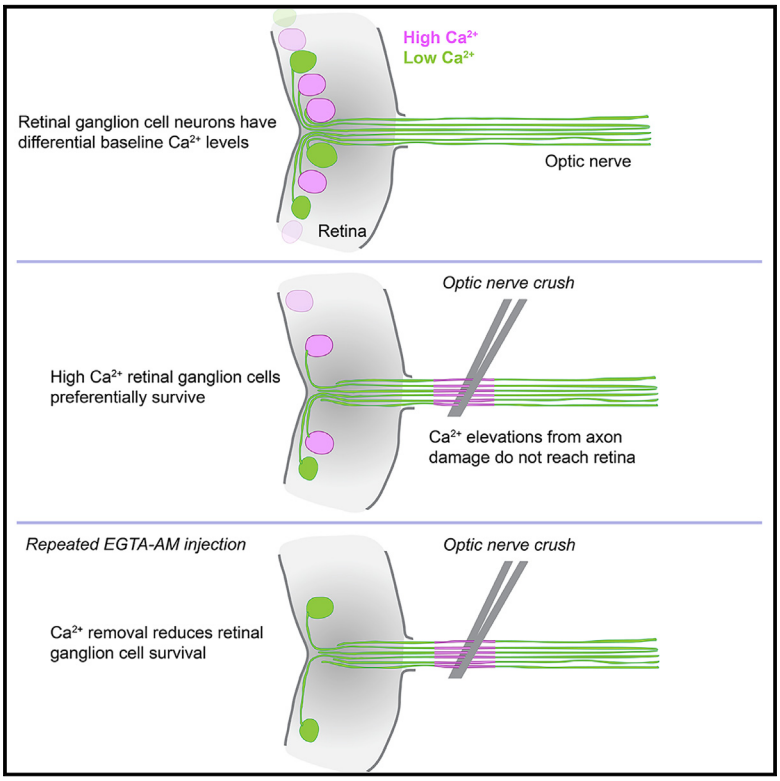

Highlights

- Retinal ganglion cells (RGCs) have differential resting Ca^{2+} levels
- Ca^{2+} elevations from axon injury do not propagate from the optic nerve to the retina
- RGCs with high resting Ca^{2+} levels survive at higher rates than those with low Ca^{2+}
- Reducing intracellular Ca^{2+} reduces RGC survival after optic nerve crush

Authors

Sean McCracken, Michael J. Fitzpatrick, Allison L. Hall, Zelun Wang, Daniel Kerschensteiner, Josh L. Morgan, Philip R. Williams

Correspondence

prwillia@wustl.edu

In brief

Elevations in homeostatic neuronal Ca^{2+} are generally associated with neurodegeneration. McCracken et al. demonstrate that Ca^{2+} levels are diverse across the retinal ganglion cell (RGC) population and that RGCs with higher resting Ca^{2+} levels are more likely to survive degeneration induced by optic nerve crush both within and across RGC types.

McCracken et al., 2023, Cell Reports *42*, 113165
October 31, 2023
https://doi.org/10.1016/j.celrep.2023.113165

CellPress

Cell Reports

CellPress
OPEN ACCESS

Report

Diversity in homeostatic calcium set points predicts retinal ganglion cell survival following optic nerve injury *in vivo*

Sean McCracken,[1,2] Michael J. Fitzpatrick,[1,2,3] Allison L. Hall,[1,4] Zelun Wang,[1,2,3] Daniel Kerschensteiner,[1,5,6,7] Josh L. Morgan,[1,5] and Philip R. Williams[1,5,6,8,*]

[1]John F. Hardesty, MD Department of Ophthalmology and Visual Sciences, Washington University School of Medicine, St. Louis, MO 63110, USA
[2]Graduate Program in Neuroscience, Washington University School of Medicine, St. Louis, MO 63110, USA
[3]Medical Scientist Training Program, Washington University School of Medicine, St. Louis, MO 63110, USA
[4]Postbaccalaureate Program in Developmental Biology & Regenerative Medicine, Washington University School of Medicine, St. Louis, MO 63110, USA
[5]Department of Neuroscience, Washington University School of Medicine, St. Louis, MO 63110, USA
[6]Hope Center for Neurological Disorders, Washington University School of Medicine, St. Louis, MO 63110, USA
[7]Department of Biomedical Engineering, Washington University School of Medicine, St. Louis, MO 63110, USA
[8]Lead contact
*Correspondence: prwillia@wustl.edu
https://doi.org/10.1016/j.celrep.2023.113165

SUMMARY

Retinal ganglion cell (RGC) degeneration drives vision loss in blinding conditions. RGC death is often triggered by axon degeneration in the optic nerve. Here, we study the contributions of dynamic and homeostatic Ca^{2+} levels to RGC death from axon injury. We find that axonal Ca^{2+} elevations from optic nerve injury do not propagate over distance or reach RGC somas, and acute and chronic Ca^{2+} dynamics do not affect RGC survival. Instead, we discover that baseline Ca^{2+} levels vary widely between RGCs and predict their survival after axon injury, and that lowering these levels reduces RGC survival. Further, we find that well-surviving RGC types have higher baseline Ca^{2+} levels than poorly surviving types. Finally, we observe considerable variation in the baseline Ca^{2+} levels of different RGCs of the same type, which are predictive of within-type differences in survival.

INTRODUCTION

Retinal ganglion cells (RGCs) are projection neurons required for vision. Damage to their axons leads to retrograde cell death and blindness in conditions including glaucoma and diffuse white matter injury.[1–4] Restoring vision in such diseases requires RGC neuroprotection. Therefore, understanding how axonal damage leads to RGC death is critical for formulating treatments that preserve RGCs.

Calcium dysregulation contributes to neuronal death in diverse neurodegenerative conditions[5–7] and contributes to RGC degeneration in different blinding diseases, including glaucoma, neuromyelitis optica, and optic nerve trauma. For example, RGC light-driven Ca^{2+} dynamics are disrupted in mouse glaucoma models.[8] Restricting Ca^{2+} influx through voltage-gated Ca^{2+} channels or AMPA channels protects RGCs from degeneration.[9,10] In contrast, increasing RGC neural activity, and presumably Ca^{2+} signaling, protects RGCs following optic nerve crush (ONC).[11–13]

Axon injury leads to Ca^{2+} elevations that drive neurodegeneration.[14–16] Optic nerve ligation causes acute Ca^{2+} elevations in RGC axons within the optic nerve that drive Wallerian-like breakdown.[17] Since axon injury is considered a catalyst for RGC degeneration in glaucoma, determining if and how Ca^{2+} signals initiated in the optic nerve affect RGC survival in the retina needs to be addressed. To investigate the role of pathological Ca^{2+} in RGC degeneration, we tracked Ca^{2+} levels acutely and chronically in RGCs following ONC in mice *in vivo*.

RESULTS

RGCs demonstrate differential baseline Ca^{2+} levels

To examine the role of Ca^{2+} in RGC degeneration, we used the fluorescence resonance energy transfer (FRET)-based Ca^{2+} biosensor Twitch2b.[18] To express Twitch2b specifically in RGCs, we delivered adeno-associated virus serotype 2 (AAV2) carrying a Cre-dependent Twitch2b expression cassette into VGlut2-Cre transgenic mice, which restricts transgene expression to RGCs and horizontal cells[13]; the latter were spatially excluded from analysis.[19] To examine RGC soma and axon Ca^{2+} levels, light-adapted mice were imaged by transpupillary 2-photon microscopy as previously described.[19] Intriguingly, we observed that RGCs displayed different Ca^{2+} levels during *in vivo* 2-photon imaging in the unperturbed state, which we will refer to as baseline throughout this report (Twitch2b ratio: 1.41 ± 0.50, mean ± SD,

1,051 RGCs from 19 retinas; Figures 1A and 1B). Axon fascicles demonstrated a lower and more uniform Ca^{2+} level distribution (Twitch2b ratio: 0.92 ± 0.13, 41 fascicles from 6 retinas). Repeat imaging the same retinal fields at 5–7 day intervals showed that RGC Ca^{2+} levels are stable (n = 225 RGCs from 4 retinas; R = 0.76; Figures 1C and 1D). Thus, RGCs demonstrate differential baseline Ca^{2+} levels that are stable in most RGCs, while axons maintain homogeneous and low Ca^{2+} levels.

Baseline Ca^{2+} levels are related to spontaneous neuronal activity

To understand the source of baseline Ca^{2+} levels in RGCs, we performed simultaneous Twitch2b measurements by low-laser-intensity 2-photon microscopy and cell-attached patch-clamp recordings in dark-adapted retinal whole mounts. We recorded spontaneous activity in RGCs for 5 min followed by 1 min recordings after KCl stimulation. Twitch2b ratios and firing rate were calculated in 5–6 s bins for each RGC. Within individual RGCs, there was a relatively strong relationship between Ca^{2+} level and firing rate (R = 0.57 ± 0.13, n = 472 bins from 8 RGCs from 4 retinas, example RGC R = 0.84; Figure 1E). In contrast, across RGCs sampled, activity only accounted for a smaller portion of the measured Ca^{2+} levels (R = 0.32; Figure 1F). Thus, modulations in neural activity shift RGC Ca^{2+} levels within individual RGCs. However, resting Ca^{2+} levels in the absence of electrical activity and the impact of electrical activity on Ca^{2+} levels are both differential across RGCs.

To determine the contribution of activity to Ca^{2+} levels *in vivo*, we recorded Twitch2b dynamics in response to intraocular delivery of tetrodotoxin (TTX) to inhibit neural circuit activity or to a cocktail of strychnine and bicuculline (S&B) to disinhibit RGCs and increase their electrical activity. We compared the response to TTX or S&B to saline vehicle control injections, which caused a reduction in RGC Ca^{2+} levels (Twitch2b change in ratio/initial ratio [ΔR/R] = −0.130 ± 0.008, n = 257 RGCs from 6 retinas). We found that administration of TTX strongly reduced RGC Ca^{2+} levels (Twitch2b ΔR/R = −0.301 ± 0.012; Figures 1G, 1H, and 1K), and 13.2% of TTX-treated RGCs demonstrated reduced Ca^{2+} levels compared to vehicle using a ΔR/R of 2 standard deviations below the mean of vehicle injections. Similarly, increasing RGC electrical activity by intravitreal S&B injection induced Ca^{2+} level elevations in RGCs (Twitch2b ΔR/R = 0.262 ± 0.014, n = 170 RGCs from 5 retinas; Figures 1I–1K), and 44.7% of S&B-treated RGCs showed increased Ca^{2+} levels compared to vehicle. Taken together, these results suggest that some RGCs have higher homeostatic Ca^{2+} set points and differential levels of spontaneous activity that are both influenced by retinal circuit activity.

While it is likely that some circuit activation is driven by our 2-photon imaging method,[20] we do not believe that laser responses distorted our baseline Ca^{2+} measurements. Previous reports have used transpupillary 2-photon imaging with similar or higher laser powers to track responses of RGCs to blue light flashes in mice *in vivo*.[21] We have also previously shown that most RGCs activated by the 2-photon laser respond with transient Ca^{2+} elevations[19] that persist for much shorter durations than our image acquisition (20 s vs. 3 min). To demonstrate that our imaging paradigm did not strongly activate RGCs, 15 min after performing transpupillary 2-photon imaging, we immunostained for c-Fos, which is rapidly upregulated in dark-adapted RGCs exposed to light.[22,23] We found that RGCs showed little c-Fos labeling in the retina as a whole following 2-photon scanning of light-adapted retinas (Figure S1A). Furthermore, comparing c-Fos levels in RGCs in the scanned region vs. RGCs away from the scanned region showed no significant difference in c-Fos expression levels (Figures S1B and S1C). Finally, *in vivo* Ca^{2+} levels were not correlated with c-Fos expression (Figures S1D–S1F), indicating that RGCs with high baseline Ca^{2+} levels are unlikely to have been driven to high activity levels by 2-photon imaging. Taken together, spontaneous or some 2-photon-driven RGC activity may influence, but does not account for, differences in RGC baseline Ca^{2+} levels that we observe with *in vivo* Twitch2b measurements.

Acute pathological Ca^{2+} elevations are not observed in the retina after optic nerve injury

Previous studies have used Twitch2b and its predecessors to demonstrate how pathological Ca^{2+} elevations drive axon degeneration across clinically relevant trauma and disease models.[15,16,24] Indeed, using a 2-photon laser spot injury within the retina, we induced axonal and somatic Ca^{2+} elevations near the laser spot that persisted for at least 60 min (Figure S2). Laser injury induced strong Ca^{2+} elevations in axons within the area of eventual degeneration, but these elevations only propagated over the first 100 μm of axons proximal to the lesion edge (Figures S2A and S2B). A similar result was observed for RGC somas where strong elevations were only observed within the degenerative field; however, smaller Ca^{2+} elevations were observed in RGCs up to 200 μm away from the edge of the lesion (Figures S2A and S2C). Thus, our *in vivo* imaging system can detect degeneration-associated changes in Ca^{2+} levels within both RGC axons and cell bodies.

To observe the possible spread of pathological Ca^{2+} after ONC, baseline Ca^{2+} images were acquired, and mice received an ONC and were imaged within 2–5 min of injury. Subsequent images were acquired every 5 min for 2–3 h (Figure 2A). Following ONC, Ca^{2+} levels in RGC axon fascicles showed no significant elevations relative to sham controls either directly after (Twitch 2b ΔR/R ONC −0.033 ± 0.019 vs. sham 0.050 ± 0.012, n = 31 axon bundles from 3 retinas for crush, 13 axon bundles from 3 retinas for sham, 95% confidence interval of the difference between means [CID] = −0.27 to −0.15) or 2 h after ONC (Twitch 2b ΔR/R ONC −0.033 ± 0.019 vs. sham 0.050 ± 0.012, 95% CID = −0.20 to 0.08; Figures 2A and 2B). Similarly, RGC somatic Ca^{2+} levels, while somewhat variable, did not increase relative to baseline and did not significantly differ from sham controls (Twitch 2b ΔR/R ONC 0.084 ± 0.024 vs. sham 0.082 ± 0.015, n = 202 RGCs from 3 retinas ONC, 133 RGCs from 3 retinas sham, 95% CID = −0.61 to 0.65; Figures 2A and 2C–2E). Since some Ca^{2+} dynamics were observed in RGC soma following ONC, we examined if acute Ca^{2+} dynamics were related to RGC survival by performing chronic imaging for 2 weeks following ONC with acute time-lapse imaging (Figure 2F). We found that acute Ca^{2+} dynamics were not different between RGCs that died or survived ONC either at the immediate time point following injury (Twitch2b ΔR/R surviving −0.01 ± 0.05 vs. dying 0.03 ± 0.03, 95%

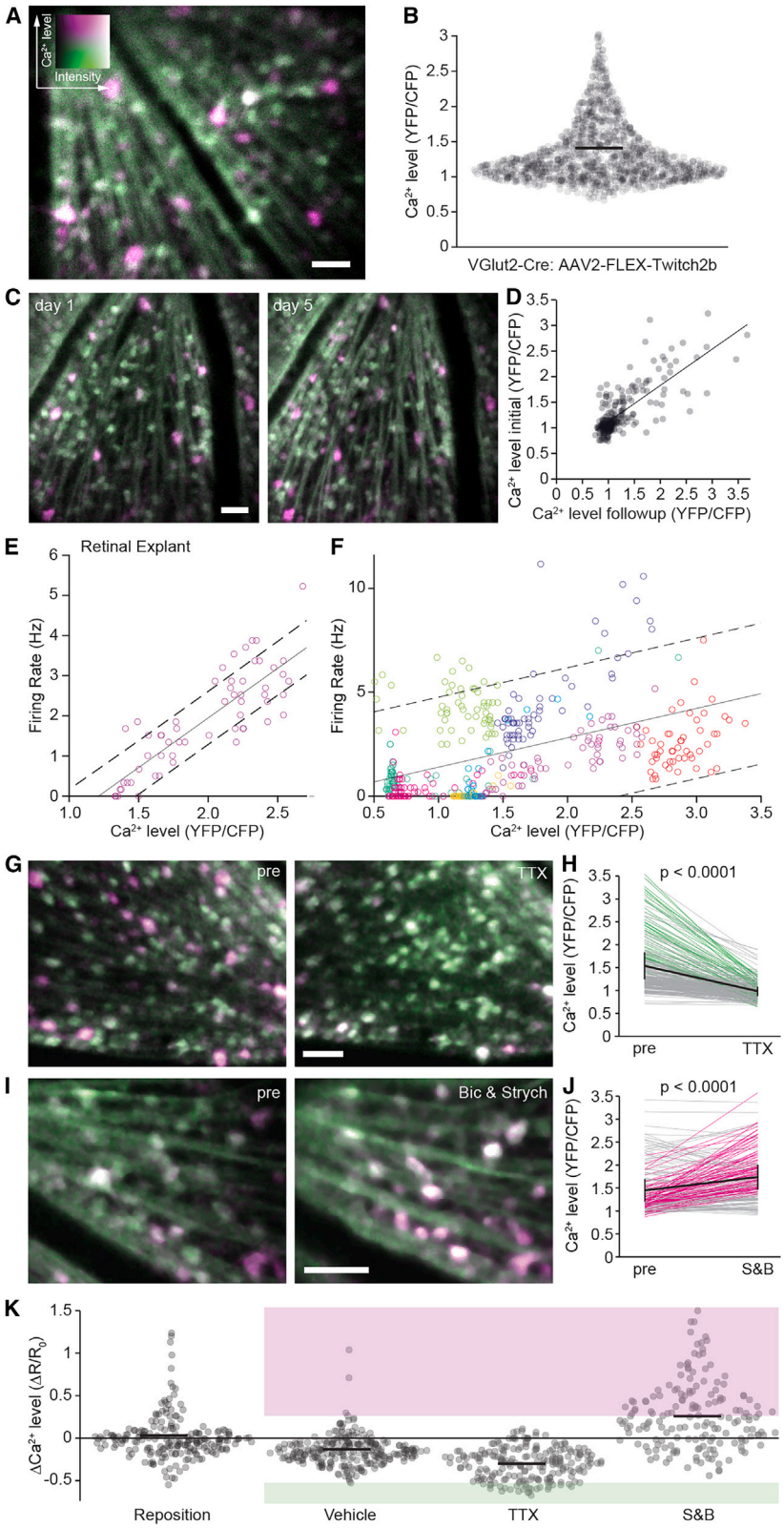

Figure 1. RGCs demonstrate differential Ca^{2+} levels

(A) *In vivo* 2-photon maximum intensity projection (mip) Twitch2b. cpVenus and mCerulean3 are pseudocolored magenta and green, respectively, throughout.

(B) Swarm plot of baseline Twitch2b ratios. Bars represent mean throughout.

(C) *In vivo* 2-photon mip of Twitch2b and imaged again 5 days later.

(D) Scatterplot of Twitch2b at baseline vs. 5–7 days later ($R = 0.76$).

(E) Twitch2b ratio vs. firing rate in an example RGC recorded from a dark adapted retinal whole mount. Each point represents an individual 6 s bin. Lines represent best fit (solid) ± 2 standard deviations from the mean (dashed) throughout.

(F) Twitch2b ratio vs. firing rate across multiple RGCs (uniquely colored).

(G) *In vivo* 2-photon mip of Twitch2b at baseline and following TTX.

(H) Line plots of individual RGCs at baseline and following TTX. Each line represents a single RGC. Green lines are significantly reduced compared to vehicle control. Heavy line shows mean and SEM throughout (paired Student's t test).

(I) *In vivo* 2-photon mip of Twitch2b at baseline and following S&B.

(H) Individual RGCs at baseline and immediately following S&B. Magenta lines are significantly increased compared to vehicle control (paired Student's t test).

(K) ΔCa^{2+} following indicated treatment. Magenta and green shaded areas are 2 SD above and below the vehicle injected mean, respectively (n = 202 RGCs from 5 retinas reposition, 260 RGCs from 5 retinas vehicle, $p < 0.0001$ for all group comparisons, one-way ANOVA multiple group comparisons with Bonferroni correction). Scale bars: 50 μm.

See also Figure S1.

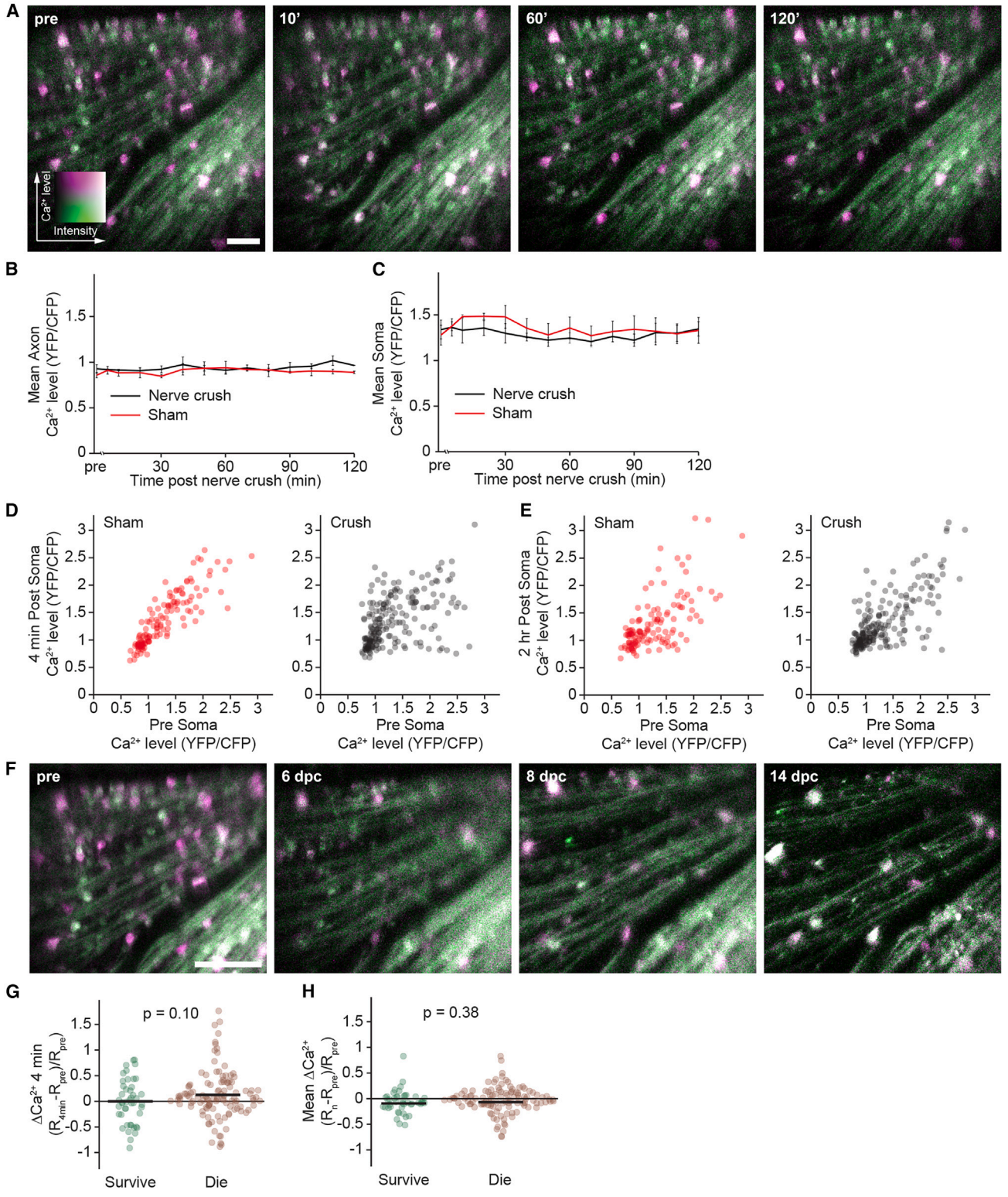

Figure 2. Acute Ca^{2+} levels are unaltered following ONC

(A) *In vivo* 2-photon mips of Twitch2b following ONC. Time in minutes.

(B) Sample mean of axon fields acute imaged in ONC (black) and sham (red) retinas. Error bars represent SEM throughout.

(C) Sample mean of RGCs following ONC and sham.

(legend continued on next page)

CID = −0.22 to 0.02, n = 160 RGCs from 3 retinas; Figure 2G) or overall across the 2 h time lapse (mean Twitch2b ΔR/R surviving −0.04 ± 0.03 vs. dying −0.05 ± 0.03, 95% CID = −0.06 to 0.07; Figure 2H). Therefore, our data suggest that acute Ca^{2+} backpropagation is not a relevant injury signal in RGCs following ONC and is unlikely to influence RGC survival.

Baseline Ca^{2+} levels correlate with RGC survival

To examine the relationship between baseline Ca^{2+} and degeneration, we tracked RGC survival following ONC after first measuring baseline Ca^{2+} levels (Figure 3A). In contrast to Ca^{2+} serving as a degenerative stimulus, we observed that surviving RGCs had higher baseline Ca^{2+} levels than dying RGCs (Twitch2b ratio surviving 1.61 ± 0.05 vs. dying 1.36 ± 0.02, n = 499 RGCs from 10 retinas; 95% CID = 0.23–0.44; Figures 3A and 3B). To determine when survival differences manifest in RGCs with different Ca^{2+} levels, we separated RGCs into "high" and "low" Ca^{2+} groups using 2 standard deviations above the TTX-treated mean as a threshold (Figures 1G, 1H, and 1K). Survival rates were relatively similar between high and low Ca^{2+} RGCs through 8 days after ONC but were significantly different from 10 days onward (n = 5 retinas including 260 RGCs; Figure 3C). By 14 days after ONC, high Ca^{2+} RGCs were 3.51 ± 0.66 times more likely to survive than their low Ca^{2+} counterparts (survival rates for high Ca^{2+} RGCs 37% ± 6.8% vs. low Ca^{2+} RGCs 11.7% ± 2.4%, 95% CID = 8.9%–41.6%; Figure 3C). To directly compare homeostatic Ca^{2+} levels with resilience, we grouped RGCs by day of death and compared their baseline Ca^{2+} levels. While all post-injury time point populations were lower than surviving RGCs, similar to the survival curve results, we found that RGCs that died on days 10 and 12 had significantly lower baseline Ca^{2+} levels than RGCs that survived to 14 days post crush (dpc; Twitch2b ratio 95% confidence interval [CI] surviving 1.56–1.85 [51 RGCs] vs. dying 4 dpc 0.12–1.92 [2 RGCs] vs. 6 dpc 1.33–1.68 [32 RGCs] vs. 8 dpc 1.38–1.63 [41 RGCs] vs. 10 dpc 1.21–1.38 [89 RGCs] vs. 12 dpc 1.17–1.52 [22 RGCs] vs. 14 dpc 1.33–1.97 [15 RGCs], n = 5 retinas). Thus, high baseline Ca^{2+} levels predict a higher likelihood of survival following ONC that does not manifest in the early stages of degeneration.

RGCs that maintain high Ca^{2+} levels are resilient to ONC

To determine how long-term Ca^{2+} dynamics might influence RGC survival, we tracked Ca^{2+} levels throughout our 14 day time lapse (Figure 3D). To examine if Ca^{2+} dynamics precede cell death, we calculated the frequency of transitions between high and low Ca^{2+} states (defined above) in the time points just prior to cell death and all other observations that did not precede RGC death. We found similar odds of Ca^{2+} elevations (low to high transitions) in the time point just before RGC death (9.9% ± 2.3%) as in all other time points of the chronic time lapse (9% ± 2.5%, n = 3 retinas including 616 transitions from 204 RGCs, 95% CID = −8.9 to 10.6). Furthermore, transitions from high to low Ca^{2+} levels were observed with probabilities similar to transitions from low to high Ca^{2+} levels at the time point preceding RGC death (high to low 12.9% ± 6.7% vs. low to high 9.9% ± 2.3%, n = 3 retinas including 616 transitions from 204 RGCs, 95% CID = −22.8 to 16.8). Calculating the population mean of Ca^{2+} levels in pre-death and non-pre-death time points, we found that Ca^{2+} levels decreased slightly at the time point just before RGC death (Twitch2b ratio ΔR/R −0.05 ± 0.03), and these dynamics were similar to Ca^{2+} changes seen in all other time points from the chronic time lapse (Twitch2b ratio ΔR/R 0.00 ± 0.01 non-dying, n = 616 transitions from 204 RGCs from 3 retinas; 95% CID = −0.11 to 0.01; Figure 3E). Taken together, Ca^{2+} dynamics in the days prior to RGC death are not related to survival following ONC.

We next examined if long-term increases in Ca^{2+} set point might protect initially low Ca^{2+} RGCs from degeneration or if Ca^{2+} decrements might remove protection from RGCs with high baseline Ca^{2+} levels. We found that RGCs with Ca^{2+} dynamics (either transitioning from high to low or low to high Ca^{2+} levels) were similarly likely to die as RGCs that always maintained low Ca^{2+} levels (survival rates high to low 19.2% ± 14.9%, low to high 19.3% ± 6.6%, and always low 13.4% ± 6%, n = 3 retinas including 204 RGCs; Figure 3F). In contrast, RGCs that maintained high Ca^{2+} levels after ONC were highly resilient with a 63.8% ± 13.9% survival rate (Figure 3F). Thus, the only condition that strongly correlated with survival was persistently high Ca^{2+} levels, which were more likely to survive than other Ca^{2+} phenotypes in RGCs.

Chelating Ca^{2+} reduces RGC survival

To examine a causative link for our observed relationship between high baseline Ca^{2+} levels and increased RGC survival after ONC, we injected the cell-permeable Ca^{2+} chelator ethyleneglycol-bis (β-aminoethyl)-N,N,N',N'-tetraacetoxymethyl ester (EGTA-AM, 1 μL 30 μM) intravitreally to reduce Ca^{2+} levels in the retina. EGTA-AM injection led to a strong reduction of Ca^{2+} levels in all RGCs (Twitch2b ΔR/R = −0.397 ± 0.018, 114 RGCs from 3 retinas; Figures 3G and 3H). Further, we observed that compared to TTX injections, EGTA-AM reduced Ca^{2+} levels to a greater extent (95% CID = −0.140 to −0.054). EGTA-AM reductions persisted for 85.2 ± 12.3 min (n = 3 retinas), as measured by the population mean returning to 90% of baseline Twitch2b ratios. Thus, EGTA-AM led to strong and lasting Ca^{2+} reductions in all RGCs.

To determine the importance of Ca^{2+} for RGC survival, we measured baseline Twitch2b ratios, performed ONC, and injected EGTA-AM intravitreally immediately after ONC and every 3 days thereafter while tracking RGC survival with *in vivo* 2-photon imaging (Figure 3I). This frequency of intermittent RGC Ca^{2+} manipulation is similar to previous experiments that increased RGC activity to promote RGC survival.[13] Importantly, injection of EGTA-AM without ONC did not cause RGC degeneration (Figure S3). Intermittent Ca^{2+} chelation with EGTA-AM led

(D) Twitch2b at baseline and first acute time point after ONC and sham (R = 0.48 ONC, R = 0.87 sham).
(E) Twitch2b at baseline and 2 h after surgery in ONC and sham (R = 0.73 ONC, R = 0.63 sham).
(F) *In vivo* 2-photon mips of Twitch2b following ONC. Same sample as in (A).
(G) ΔCa^{2+} between baseline and first acute time point in RGCs that survived (green) and died (red; Student's t test). Bars represent mean throughout.
(H) Mean ΔCa^{2+} between baseline and all acute time points (as graphed in C) in RGCs that survived and died. Scale bars: 50 μm.
See also Figure S2.

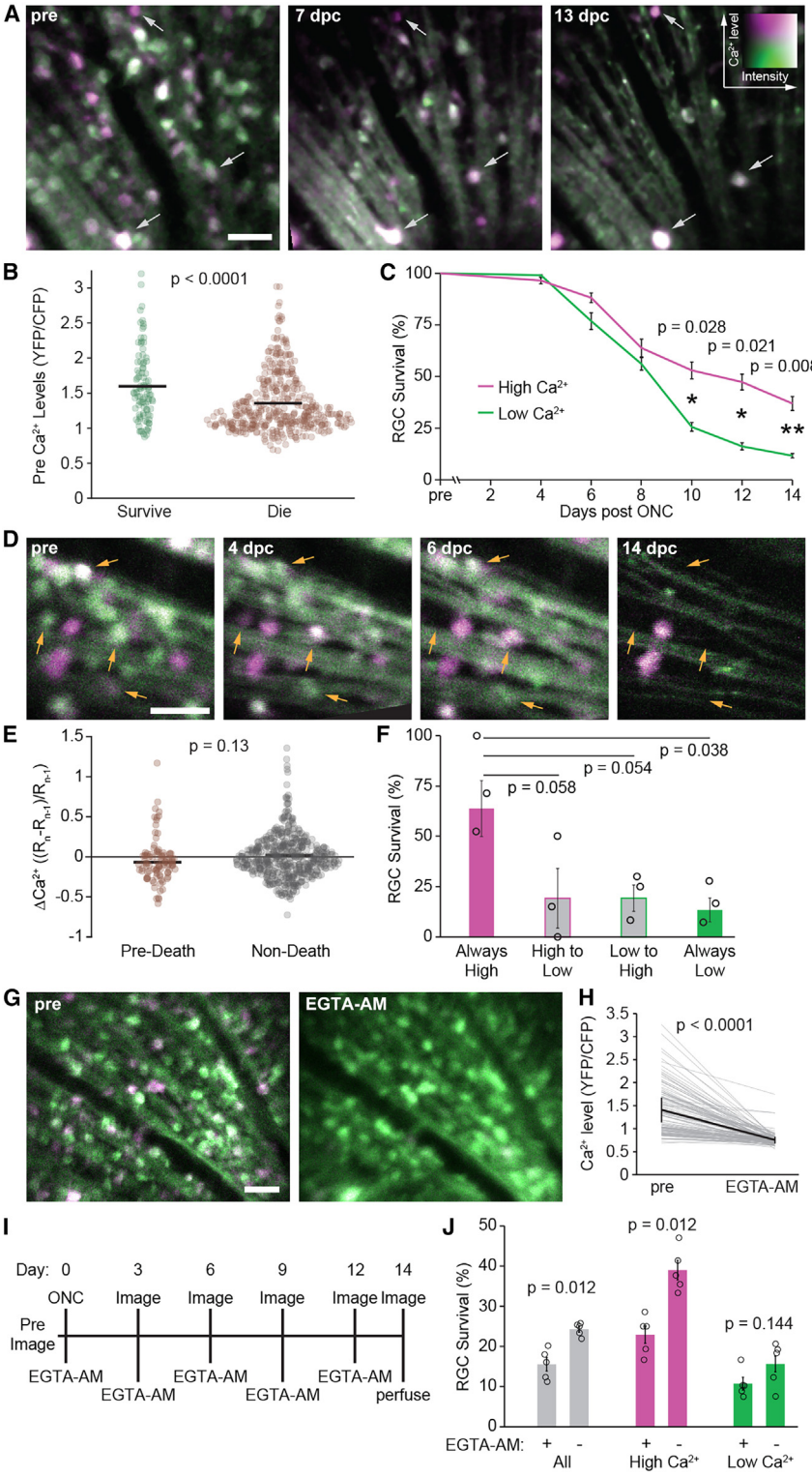

Figure 3. High Ca^{2+} levels are correlated with RGC survival

(A) *In vivo* 2-photon mips of Twitch2b at indicated days following ONC. Arrows indicate surviving high Ca^{2+} RGCs.

(B) Baseline Twitch2b in RGCs that survived (green) and died (red; Student's t test). Bars represent mean throughout.

(C) Survival curves of RGCs with high (magenta) or low (green) baseline Ca^{2+} (Mann Whitney U test). Error bars represent SEM throughout.

(D) *In vivo* 2-photon mips of Twitch2b at indicated days following ONC. Arrows indicate dying RGCs with Ca^{2+} levels that change.

(E) ΔCa^{2+} just prior to RGC death (red) and all other time points (gray; Student's t test).

(F) Percentage of surviving RGCs with indicated chronic Ca^{2+} dynamics. Bars represent mean and points indicate individual retinas (one-way ANOVA with Bonferroni correction).

(G) *In vivo* 2-photon mips of Twitch2b at baseline and after EGTA-AM.

(H) Individual RGCs at baseline and following EGTA-AM. Each line represents a single RGC, heavy line represents mean and SEM (paired Student's t test).

(I) Timeline of EGTA-AM experiments.

(J) Percentage of surviving RGCs classed by baseline Ca^{2+} levels compared between vehicle and EGTA-AM treatments (one-way ANOVA with Bonferroni correction). Points represent individual retinae, bars represent mean. Scale bars: 50 μm. See also Figure S3.

to a significant reduction in RGC survival (EGTA-AM 15.6% ± 3.8% vs. vehicle 24.3% ± 1.6%, 95% CID = −13.3% to −4.1%, n = 5 retinas including 547 RGCs and 5 retinas including 607 RGCs, respectively; Figure 3J). Examining the effects of Ca^{2+} chelation on RGC survival across high or low Ca^{2+} RGCs showed that high Ca^{2+} RGC survival was more strongly reduced by EGTA-AM treatment than low Ca^{2+} RGC survival (high Ca^{2+} EGTA-AM 22.9% ± 4.8% vs. vehicle 39% ± 5.4%, 95% CID = −23.5% to −8.6%, n = 5 retinas including 218 RGCs and 5 retinas including 208 RGCs, respectively; low Ca^{2+} EGTA-AM 10.7% ± 3.5% vs. vehicle 15.6% ± 5.5%, 95% CID = −11.9% to 2%, n = 329 RGCs from 5 retinas and 399 RGCs from 5 retinas, respectively; Figure 3J). Taken together, these experiments suggest that the maintenance of high Ca^{2+} levels is an important feature for the survival of natively resilient RGCs, especially those that demonstrate high baseline Ca^{2+} levels.

Well-surviving RGC types have high baseline Ca^{2+} levels

The mouse retina contains about 45 different types of RGCs that can be differentiated by gene expression, electrophysiological responses to light, dendritic morphology, and brain projections.[25–27] Importantly, these RGC types differ in their vulnerability to ONC and other forms of degeneration.[27–32] Thus, high baseline Ca^{2+} levels could be a specific feature of resilient RGC types, and/or

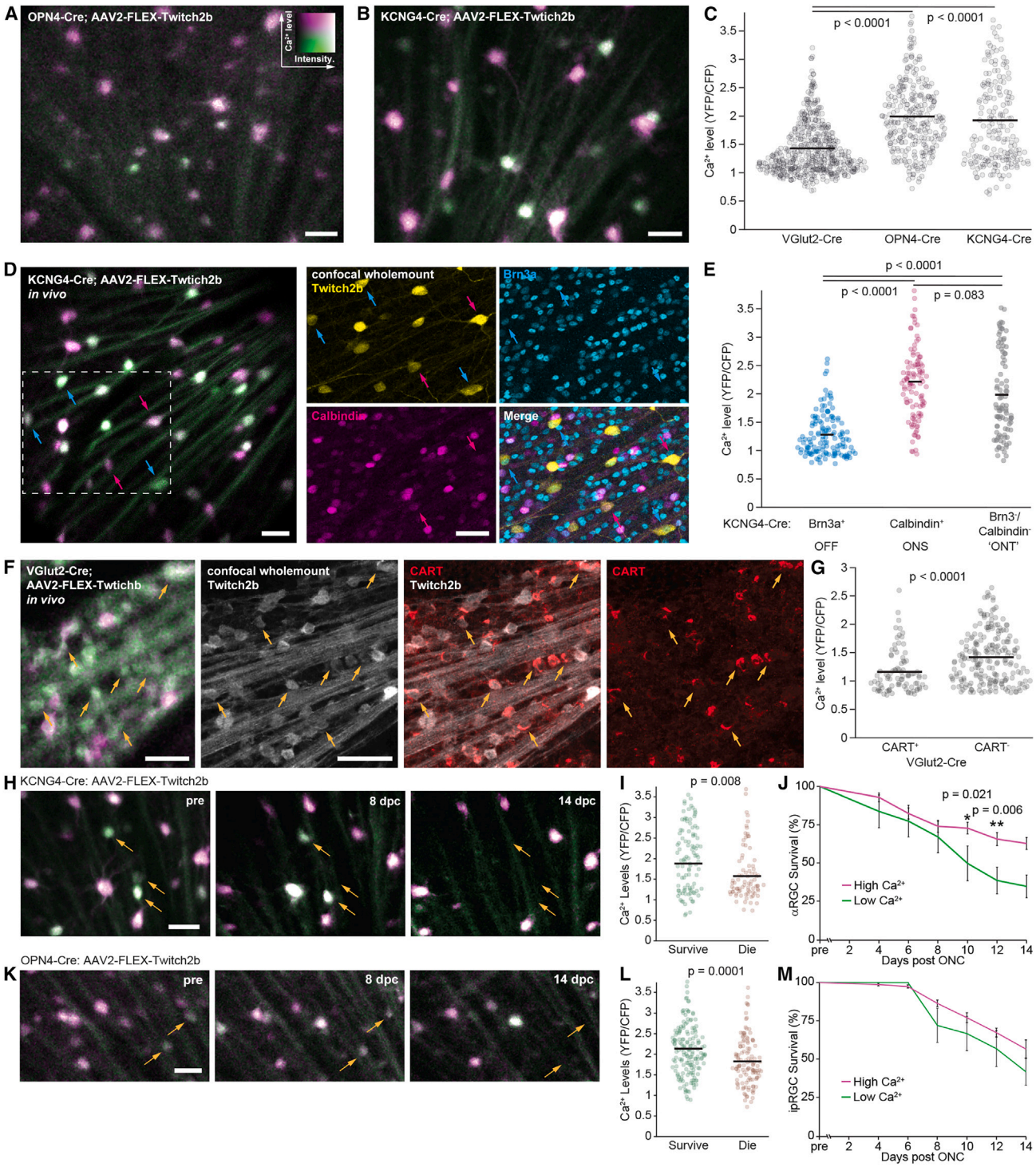

Figure 4. Well-surviving RGC types have higher baseline Ca^{2+} levels that predict survival

(A and B) *In vivo* 2-photon mip of Twitch2b in (A) ipRGCs (OPN4-Cre) and (B) αRGCs (KCNG4-Cre).

(C) Twitch2b ratios in all RGCs (VGlut2-Cre; re-graphed from Figure 2B), ipRGCs, and αRGCs (Student's t test). Bars represent mean throughout.

(D) *In vivo* 2-photon mip of Twitch2b αRGCs and *ex vivo* confocal mips of Brn3a (cyan) and calbindin (magenta) immunostaining and Twitch2b (yellow) in fixed whole mounts. Box indicates area shown in confocal whole mount. Arrows indicate immunopositive RGCs.

(E) Twitch2b ratios in Brn3a+, calbindin+, and Brn3a−/calbindin− RGCs (ANOVA with Bonferroni correction).

(legend continued on next page)

baseline Ca^{2+} levels could be predictive of survival independent of and within RGC types. To investigate this relationship, we expressed Twitch2b in two transgenic mouse lines enriched for well-surviving RGCs: KCNG4-Cre (αRGCs[31]) and OPN4-Cre (intrinsically photosensitive RGCs [ipRGCs][33]). We found that baseline Ca^{2+} levels were higher in both of these transgenic lines compared with all RGCs labeled in VGlut2-Cre transgenic mice (Twitch2b ratios of KCNG4 1.86 ± 0.77, mean ± SD, n = 196 RGCs form 9 retinas, OPN4 2.01 ± 0.63, n = 282 RGCs from 11 retinas vs. VGlut2 1.41 ± 0.50, 1051 RGCs from 19 retinas; Figures 4A–4C). Since αRGCs and ipRGCs are families that represent multiple specific RGC types, we performed immunostaining for more specific RGC types after *in vivo* Twitch2b imaging within the KCNG4-Cre transgenic mice. We labeled ON-sustained αRGCs (ONSαRGCs) with calbindin and OFF-sustained and OFF-transient αRGCs with Brn3a (OFFαRGCs), while the remaining unlabeled "other" αRGCs are likely to be heavily enriched for ON-transient αRGCs.[34] We found that OFFαRGCs (Twitch2b ratio 1.28 ± 0.38, mean ± SD, 134 RGCs from 5 retinas) had significantly lower Ca^{2+} levels than either ONSαRGCs (2.21 ± 0.68, 109 RGCs) or presumed ONTαRGCs (1.98 ± 0.76, 96 RGCs, $p < 0.0001$, ANOVA with Bonferroni correction; Figures 4D and 4E).

To examine a poorly surviving RGC type, we performed *in vivo* Twitch2b imaging in VGlut2-Cre transgenic mice followed by immunostaining for (cocaine- and amphetamine-regulated transcript [CART]), a marker enriched in ON-OFF-direction-selective RGCs (ooDS-RGCs[35]; Figure 4F). CART-expressing RGCs exhibited lower baseline Ca^{2+} levels than their CART-negative counterparts (Twitch2b ratios of CART+ 1.16 ± 0.37, mean ± SD vs. CART− 1.42 ± 0.45, n = 300 RGCs from 3 retinas, 95% CID = 0.15–0.36; Figures 4F and 4G). Thus, high baseline Ca^{2+} is a feature of RGC types that are well surviving, while low baseline Ca^{2+} levels are found in RGC types that are poorly surviving.

Ca^{2+} levels correlate with RGC survival within restricted RGC types

To determine if baseline Ca^{2+} also controls survival within a similar cohort of RGCs, we tracked the relationship between baseline Ca^{2+} and survival following ONC in KCNG4-Cre and OPN4-Cre transgenic mice. In KCNG4-Cre mice, αRGCs that survived ONC had significantly higher baseline Ca^{2+} levels than αRGCs that died (Twitch2b ratios of surviving 2 ± 0.08 vs. dying 1.70 ± 0.09, 95% CID = 0.08–0.53, n = 196 αRGCs from 9 retinas; Figures 4H and 4I). Additionally, high baseline Ca^{2+} αRGCs were 57.6% ± 15.3% more likely to survive at 14 days than low Ca^{2+} αRGCs (survival rates for high Ca^{2+} αRGCs 62.9% ± 3.9% vs. low Ca^{2+} αRGCs 35% ± 7.4%, 95% CID = 10.2%–45.6%, n = 9 retinas including 196 RGCs; Figure 4J). In OPN4-Cre transgenic mice, ipRGCs that survived ONC had significantly higher baseline Ca^{2+} levels than ipRGCs that died by 14 days (Twitch2b ratios surviving 2.13 ± 0.05 vs. dying 1.83 ± 0.05, 95% CID = 0.15–0.45, n = 282 ipRGCs from 11 retinas; Figures 4K and 4L). And while we did find a trend for increased survival (44.5% ± 35.3%) for high Ca^{2+} ipRGCs compared with low Ca^{2+} ipRGCs at 14 days after crush, this result was statistically not significant (survival rates for high Ca^{2+} ipRGCs 56.7% ± 5.9% vs. low Ca^{2+} ipRGCs 41.9% ± 8.8%, mean ± SEM, 95% CID = −8% to 37.6%, n = 11 retinas including 282 ipRGCs; Figure 4M), possibly due to the low proportion of low Ca^{2+} ipRGCs in the OPN4-Cre transgenic mouse (15.7% ± 5.6%). Thus, baseline Ca^{2+} controls survival both across and within RGC types.

DISCUSSION

In this study, we demonstrate that *in vivo* biosensor imaging can link cellular traits to degenerative outcome. We describe heterogeneity in baseline Ca^{2+} levels across all RGCs and show that RGC types differ in their population means and that even within an RGC type, baseline Ca^{2+} levels vary widely. Although both acute and chronic disturbances in Ca^{2+} homeostasis can drive neuronal degeneration in traumatic[14,15,17] and disease models,[5–7,9,16,24] the influence of homeostatic Ca^{2+} set points in individual neurons remains unclear. We found that RGCs with high baseline Ca^{2+} were more likely to survive after axotomy, within and across RGC types, and that lowering these higher baseline Ca^{2+} levels reduces RGC survival. This contrasts with observations in RGC axons, where Ca^{2+} elevation drives axonal fragmentation after optic nerve ligation.[17] Our findings also contrast with multiple models of disease and excitotoxicity where aberrant increases in intracellular Ca^{2+} drive neuronal death.[5–7,9,14] But the importance of high Ca^{2+} levels in protecting RGCs supports previous reports of greater survival with increased RGC electrical activity.[11–13]

While axonal Ca^{2+} has been studied in relation to axonal fragmentation in the CNS *in vivo,*[15–17,36,37] the implications of Ca^{2+} for retrograde neuronal degeneration remain unclear. The lack of acute Ca^{2+} backpropagation into retinal axons following ONC suggests that Ca^{2+} signaling is not relevant to the RGC response to axon injury. It is possible that a brief Ca^{2+} elevation evaded our imaging paradigm.[17] However, local retina laser injury led to Ca^{2+} elevations in axon fascicles and soma for at least tens of minutes, albeit only over about 200 μm distance. Ca^{2+} spreading after rat optic nerve ligation was only examined close to the lesion site (50–120 μm). Myelination can also influence Ca^{2+} propagation in axons. Following spinal cord injury, myelinated axons halt Ca^{2+} propagation[15] and fragmentation[38]

(F) *In vivo* 2-photon mip of Twitch2b in RGCs and *ex vivo* confocal mips of CART immunostaining (red) and Twitch2b (grayscale) in fixed whole mount. Arrows indicate CART+ RGCs.
(G) Twitch2b ratios in CART+ and CART− RGCs (Student's t test).
(H) *In vivo* 2-photon mips of Twitch2b at indicated days following ONC in αRGCs.
(I) Ca^{2+} levels in αRGCs that survived (green) and died (red) (Student's t test).
(J) Survival curves of αRGCs with high (magenta) and low (green) Ca^{2+} levels (Mann-Whitney U test). Error bars represent SEM throughout.
(K) *In vivo* 2-photon mips of Twitch2b at indicated days following ONC in ipRGCs.
(L) Ca^{2+} levels in ipRGCs that survived and died. Bars represent mean.
(M) Survival curves of ipRGCs with high (magenta) and low (green) Ca^{2+} levels. Scale bars: 50 μm.

at nodes of Ranvier and branch points. However, thin unmyelinated C-fibers show variable spatiotemporal Ca^{2+} dynamics that can be temporally uncoupled from dystrophic morphology,[15] similar to neuromyelitis optica.[24] Since RGC axons are myelinated in the optic nerve, but not in the retina, this transition could regulate Ca^{2+} spread following axon damage in the optic nerve.

Finding that RGCs with high Ca^{2+} are more likely to survive is intriguing since elevated Ca^{2+} is traditionally associated with degeneration.[5–7,14–17] Comparing our Twitch2b ratio distributions with previously published standard curves,[18] our threshold for high- vs. low-Ca^{2+}-classified RGCs is likely between 100 and 200 nM Ca^{2+}. Thus, neural activity likely contributes to baseline Ca^{2+} levels in many of our RGCs with higher Ca^{2+}, especially those with ratios near the maximum range of Twitch2b. Indeed, well-surviving RGC types have higher spontaneous firing rates (sustained αRGCs[39,40]) or are capable of prolonged bouts of activity (ipRGCs[41]) and possess higher baseline Ca^{2+} levels. While we observed that baseline Ca^{2+} predicted survival across αRGCs or ipRGCs, unfortunately, specific type marker antibodies performed were not reliable after ONC to disambiguate survival of specific RGC types.

In this study, we also found that altering retinal circuit activity by inhibiting or promoting RGC firing was differentially effective at changing Ca^{2+} levels across the RGC population and that reducing circuit activity could not reduce Ca^{2+} in RGCs to the extent of EGTA-AM. Furthermore, we show that different RGCs can have different Ca^{2+} levels when not spiking or when spike rates are similar. Thus, both differential Ca^{2+} levels, irrespective of neural activity, or differential impact and persistence of Ca^{2+} from retinal circuit activity could establish baseline levels observed in RGCs. The connection between Ca^{2+} and RGC survival remains unclear. ONC reduces CaMKII signaling, and significant protection of RGCs is achieved by overexpressing constitutively active CaMKII.[42] We examined if CaMKII signaling might link Ca^{2+} levels to RGC survival by observing Ca^{2+} levels and CaMKII, pCaMKII, and pCREB expression in the same RGCs. However, we did not find any relationship between Twitch2b ratios and immunofluorescence intensity for CaMKII, pCAMKII, or pCREB in healthy or injured RGCs (Figure S4). The fact that we observed homeostatic Ca^{2+} levels were only predictive of survival differences at later time points after ONC and relay partial protection also suggests that increased CamKII signaling, which is highly protective,[14] likely represents a different mechanism than what we describe here. Thus, we believe that other mechanisms link higher Ca^{2+} levels to native RGC survival. Taken together, our data demonstrate a clear relationship between well-surviving RGCs and baseline Ca^{2+} levels within and across RGC types.

Limitations of the study

A major challenge of studying the retina with imaging-based techniques is the inherent stimulation of retinal circuits induced by light. While these effects are likely decreased using 2-photon microscopy, it is likely that the Ca^{2+} measurements we report are a combination of differential homeostatic set points, spontaneous activity, and 2-photon-mediated stimulation. Additionally, our use of EGTA-AM to decrease Ca^{2+} across RGCs will certainly alter Ca^{2+} levels throughout the retina and eye. Future experiments are warranted to demonstrate a direct effect of exclusively reducing RGC Ca^{2+} levels and to further clarify which Ca^{2+} sources critically influence survival.

STAR★METHODS

Detailed methods are provided in the online version of this paper and include the following:

- KEY RESOURCES TABLE
- RESOURCE AVAILABILITY
  - Lead contact
  - Materials availability
  - Data and code availability
- EXPERIMENTAL MODEL AND SUBJECT DETAILS
  - Animals
- METHOD DETAILS
  - Intravitreal AAV injections
  - *In vivo* imaging of mouse retinal ganglion cells
  - Injury models
  - *In vivo* imaging analysis
  - Perfusions and Tissue preparation
  - Retinal wholemount immunostaining
  - Confocal microscopy
  - Electrophysiology
  - Electrophysiology analysis
- QUANTIFICATION AND STATISTICAL ANALYSIS

SUPPLEMENTAL INFORMATION

Supplemental information can be found online at https://doi.org/10.1016/j.celrep.2023.113165.

ACKNOWLEDGMENTS

We thank Christopher Zhao, Li Huang, Shelly Xu, Michael Casey, and Mingjie Li for assistance. S.M. and Z.W. were supported by an Institutional National Research Service Award T32 EY013360. This work was supported by grants from Research to Prevent Blindness (Career Development Award, P.R.W. and J.L.M.); the BrightFocus Foundation (National Glaucoma Research, P.R.W.); the Alcon Research Institute (Young Investigator Award to P.R.W.); and NIH grants (EY032908to P.R.W.; EY027411, EY034001, and EY026978to D.K.; and EYE030623 and EY029313 to J.L.M.). This work was supported by the Hope Center Viral Vectors Core at Washington University School of Medicine, an unrestricted grant (to the Department of Ophthalmology and Visual Sciences) from Research to Prevent Blindness, and Vision Core Grant P30 EY002687.

AUTHOR CONTRIBUTIONS

S.M., D.K., J.L.M., and P.R.W. conceived and designed experiments. S.M., M.J.F., A.L.H., Z.W., and P.R.W. performed experiments and analyzed data. D.K., J.L.M., and P.R.W. provided supervision and funding. S.M. and P.R.W. wrote the paper with input from all authors.

DECLARATION OF INTERESTS

D.K. is a member of the *Cell Reports* scientific advisory board.

INCLUSION AND DIVERSITY

We support inclusive, diverse, and equitable conduct of research.

Received: October 17, 2022
Revised: June 29, 2023
Accepted: September 7, 2023

REFERENCES

1. Carelli, V., La Morgia, C., Ross-Cisneros, F.N., and Sadun, A.A. (2017). Optic neuropathies: the tip of the neurodegeneration iceberg. Hum. Mol. Genet. *26*, R139–R150. https://doi.org/10.1093/hmg/ddx273.
2. Levin, L.A. (1997). Mechanisms of optic neuropathy. Curr. Opin. Ophthalmol. *8*, 9–15. https://doi.org/10.1097/00055735-199712000-00003.
3. Quigley, H.A. (2016). Understanding Glaucomatous Optic Neuropathy: The Synergy Between Clinical Observation and Investigation. Annu. Rev. Vis. Sci. *2*, 235–254. https://doi.org/10.1146/annurev-vision-111815-114417.
4. Williams, P.R., Benowitz, L.I., Goldberg, J.L., and He, Z. (2020). Axon Regeneration in the Mammalian Optic Nerve. Annu. Rev. Vis. Sci. *6*, 195–213. https://doi.org/10.1146/annurev-vision-022720-094953.
5. Calvo-Rodriguez, M., Hou, S.S., Snyder, A.C., Kharitonova, E.K., Russ, A.N., Das, S., Fan, Z., Muzikansky, A., Garcia-Alloza, M., Serrano-Pozo, A., et al. (2020). Increased mitochondrial calcium levels associated with neuronal death in a mouse model of Alzheimer's disease. Nat. Commun. *11*, 2146. https://doi.org/10.1038/s41467-020-16074-2.
6. Gandhi, S., Wood-Kaczmar, A., Yao, Z., Plun-Favreau, H., Deas, E., Klupsch, K., Downward, J., Latchman, D.S., Tabrizi, S.J., Wood, N.W., et al. (2009). PINK1-associated Parkinson's disease is caused by neuronal vulnerability to calcium-induced cell death. Mol. Cell *33*, 627–638. https://doi.org/10.1016/j.molcel.2009.02.013.
7. Tu, H., Nelson, O., Bezprozvanny, A., Wang, Z., Lee, S.F., Hao, Y.H., Serneels, L., De Strooper, B., Yu, G., and Bezprozvanny, I. (2006). Presenilins form ER Ca2+ leak channels, a function disrupted by familial Alzheimer's disease-linked mutations. Cell *126*, 981–993. https://doi.org/10.1016/j.cell.2006.06.059.
8. Quintero, H., Shiga, Y., Belforte, N., Alarcon-Martinez, L., El Hajji, S., Villafranca-Baughman, D., Dotigny, F., and Di Polo, A. (2022). Restoration of mitochondria axonal transport by adaptor Disc1 supplementation prevents neurodegeneration and rescues visual function. Cell Rep. *40*, 111324. https://doi.org/10.1016/j.celrep.2022.111324.
9. Karim, Z., Sawada, A., Kawakami, H., Yamamoto, T., and Taniguchi, T. (2006). A new calcium channel antagonist, lomerizine, alleviates secondary retinal ganglion cell death after optic nerve injury in the rat. Curr. Eye Res. *31*, 273–283. https://doi.org/10.1080/02713680500536647.
10. Cueva Vargas, J.L., Osswald, I.K., Unsain, N., Aurousseau, M.R., Barker, P.A., Bowie, D., and Di Polo, A. (2015). Soluble Tumor Necrosis Factor Alpha Promotes Retinal Ganglion Cell Death in Glaucoma via Calcium-Permeable AMPA Receptor Activation. J. Neurosci. *35*, 12088–12102. https://doi.org/10.1523/JNEUROSCI.1273-15.2015.
11. Li, S., Yang, C., Zhang, L., Gao, X., Wang, X., Liu, W., Wang, Y., Jiang, S., Wong, Y.H., Zhang, Y., and Liu, K. (2016). Promoting axon regeneration in the adult CNS by modulation of the melanopsin/GPCR signaling. Proc. Natl. Acad. Sci. USA *113*, 1937–1942. https://doi.org/10.1073/pnas.1523645113.
12. Lim, J.H.A., Stafford, B.K., Nguyen, P.L., Lien, B.V., Wang, C., Zukor, K., He, Z., and Huberman, A.D. (2016). Neural activity promotes long-distance, target-specific regeneration of adult retinal axons. Nat. Neurosci. *19*, 1073–1084. https://doi.org/10.1038/nn.4340.
13. Zhang, Y., Williams, P.R., Jacobi, A., Wang, C., Goel, A., Hirano, A.A., Brecha, N.C., Kerschensteiner, D., and He, Z. (2019). Elevating Growth Factor Responsiveness and Axon Regeneration by Modulating Presynaptic Inputs. Neuron *103*, 39–51.e5. https://doi.org/10.1016/j.neuron.2019.04.033.
14. Büki, A., Siman, R., Trojanowski, J.Q., and Povlishock, J.T. (1999). The role of calpain-mediated spectrin proteolysis in traumatically induced axonal injury. J. Neuropathol. Exp. Neurol. *58*, 365–375. https://doi.org/10.1097/00005072-199904000-00007.
15. Williams, P.R., Marincu, B.N., Sorbara, C.D., Mahler, C.F., Schumacher, A.M., Griesbeck, O., Kerschensteiner, M., and Misgeld, T. (2014). A recoverable state of axon injury persists for hours after spinal cord contusion in vivo. Nat. Commun. *5*, 5683. https://doi.org/10.1038/ncomms6683.
16. Witte, M.E., Schumacher, A.M., Mahler, C.F., Bewersdorf, J.P., Lehmitz, J., Scheiter, A., Sánchez, P., Williams, P.R., Griesbeck, O., Naumann, R., et al. (2019). Calcium Influx through Plasma-Membrane Nanoruptures Drives Axon Degeneration in a Model of Multiple Sclerosis. Neuron *101*, 615–624.e5. https://doi.org/10.1016/j.neuron.2018.12.023.
17. Knöferle, J., Koch, J.C., Ostendorf, T., Michel, U., Planchamp, V., Vutova, P., Tönges, L., Stadelmann, C., Brück, W., Bähr, M., and Lingor, P. (2010). Mechanisms of acute axonal degeneration in the optic nerve in vivo. Proc. Natl. Acad. Sci. USA *107*, 6064–6069. https://doi.org/10.1073/pnas.0909794107.
18. Thestrup, T., Litzlbauer, J., Bartholomäus, I., Mues, M., Russo, L., Dana, H., Kovalchuk, Y., Liang, Y., Kalamakis, G., Laukat, Y., et al. (2014). Optimized ratiometric calcium sensors for functional in vivo imaging of neurons and T lymphocytes. Nat. Methods *11*, 175–182. https://doi.org/10.1038/nmeth.2773.
19. Wang, Z., McCracken, S., and Williams, P.R. (2021). Transpupillary Two-photon In vivo Imaging of the Mouse Retina. J. Vis. Exp. https://doi.org/10.103791/61970.
20. Euler, T., Hausselt, S.E., Margolis, D.J., Breuninger, T., Castell, X., Detwiler, P.B., and Denk, W. (2009). Eyecup scope–optical recordings of light stimulus-evoked fluorescence signals in the retina. Pflügers Archiv *457*, 1393–1414. https://doi.org/10.1007/s00424-008-0603-5.
21. Qin, Z., He, S., Yang, C., Yung, J.S.Y., Chen, C., Leung, C.K.S., Liu, K., and Qu, J.Y. (2020). Adaptive optics two-photon microscopy enables near-diffraction-limited and functional retinal imaging in vivo. Light Sci. Appl. *9*, 79. https://doi.org/10.1038/s41377-020-0317-9.
22. Yoshida, K., Kawamura, K., and Imaki, J. (1993). Differential expression of c-fos mRNA in rat retinal cells: regulation by light/dark cycle. Neuron *10*, 1049–1054. https://doi.org/10.1016/0896-6273(93)90053-t.
23. Hanzlicek, B.W., Peachey, N.S., Grimm, C., Hagstrom, S.A., and Ball, S.L. (2004). Probing inner retinal circuits in the rod pathway: a comparison of c-fos activation in mutant mice. Vis. Neurosci. *21*, 873–881. https://doi.org/10.1017/S0952523804216078.
24. Herwerth, M., Kenet, S., Schifferer, M., Winkler, A., Weber, M., Snaidero, N., Wang, M., Lohrberg, M., Bennett, J.L., Stadelmann, C., et al. (2022). A new form of axonal pathology in a spinal model of neuromyelitis optica. Brain *145*, 1726–1742. https://doi.org/10.1093/brain/awac079.
25. Rheaume, B.A., Jereen, A., Bolisetty, M., Sajid, M.S., Yang, Y., Renna, K., Sun, L., Robson, P., and Trakhtenberg, E.F. (2018). Single cell transcriptome profiling of retinal ganglion cells identifies cellular subtypes. Nat. Commun. *9*, 2759. https://doi.org/10.1038/s41467-018-05134-3.
26. Sanes, J.R., and Masland, R.H. (2015). The types of retinal ganglion cells: current status and implications for neuronal classification. Annu. Rev. Neurosci. *38*, 221–246. https://doi.org/10.1146/annurev-neuro-071714-034120.
27. Tran, N.M., Shekhar, K., Whitney, I.E., Jacobi, A., Benhar, I., Hong, G., Yan, W., Adiconis, X., Arnold, M.E., Lee, J.M., et al. (2019). Single-Cell Profiles of Retinal Ganglion Cells Differing in Resilience to Injury Reveal Neuroprotective Genes. Neuron *104*, 1039–1055.e12.e1012. https://doi.org/10.1016/j.neuron.2019.11.006.
28. Glovinsky, Y., Quigley, H.A., and Dunkelberger, G.R. (1991). Retinal ganglion cell loss is size dependent in experimental glaucoma. Invest. Ophthalmol. Vis. Sci. *32*, 484–491.
29. Kerrigan-Baumrind, L.A., Quigley, H.A., Pease, M.E., Kerrigan, D.F., and Mitchell, R.S. (2000). Number of ganglion cells in glaucoma eyes compared with threshold visual field tests in the same persons. Invest. Ophthalmol. Vis. Sci. *41*, 741–748.
30. Daniel, S., Clark, A.F., and McDowell, C.M. (2018). Subtype-specific response of retinal ganglion cells to optic nerve crush. Cell Death Dis. *4*, 7. https://doi.org/10.1038/s41420-018-0069-y.

31. Duan, X., Qiao, M., Bei, F., Kim, I.J., He, Z., and Sanes, J.R. (2015). Subtype-specific regeneration of retinal ganglion cells following axotomy: effects of osteopontin and mTOR signaling. Neuron *85*, 1244–1256. https://doi.org/10.1016/j.neuron.2015.02.017.

32. Della Santina, L., Inman, D.M., Lupien, C.B., Horner, P.J., and Wong, R.O.L. (2013). Differential progression of structural and functional alterations in distinct retinal ganglion cell types in a mouse model of glaucoma. J. Neurosci. *33*, 17444–17457. https://doi.org/10.1523/JNEUROSCI.5461-12.2013.

33. Ecker, J.L., Dumitrescu, O.N., Wong, K.Y., Alam, N.M., Chen, S.K., LeGates, T., Renna, J.M., Prusky, G.T., Berson, D.M., and Hattar, S. (2010). Melanopsin-expressing retinal ganglion-cell photoreceptors: cellular diversity and role in pattern vision. Neuron *67*, 49–60. https://doi.org/10.1016/j.neuron.2010.05.023.

34. Krieger, B., Qiao, M., Rousso, D.L., Sanes, J.R., and Meister, M. (2017). Four alpha ganglion cell types in mouse retina: Function, structure, and molecular signatures. PLoS One *12*, e0180091. https://doi.org/10.1371/journal.pone.0180091.

35. Kay, J.N., De la Huerta, I., Kim, I.J., Zhang, Y., Yamagata, M., Chu, M.W., Meister, M., and Sanes, J.R. (2011). Retinal ganglion cells with distinct directional preferences differ in molecular identity, structure, and central projections. J. Neurosci. *31*, 7753–7762. https://doi.org/10.1523/JNEUROSCI.0907-11.2011.

36. Breckwoldt, M.O., Pfister, F.M.J., Bradley, P.M., Marinković, P., Williams, P.R., Brill, M.S., Plomer, B., Schmalz, A., St Clair, D.K., Naumann, R., et al. (2014). Multiparametric optical analysis of mitochondrial redox signals during neuronal physiology and pathology in vivo. Nat. Med. *20*, 555–560. https://doi.org/10.1038/nm.3520.

37. Vargas, M.E., Yamagishi, Y., Tessier-Lavigne, M., and Sagasti, A. (2015). Live Imaging of Calcium Dynamics during Axon Degeneration Reveals Two Functionally Distinct Phases of Calcium Influx. J. Neurosci. *35*, 15026–15038. https://doi.org/10.1523/JNEUROSCI.2484-15.2015.

38. Lorenzana, A.O., Lee, J.K., Mui, M., Chang, A., and Zheng, B. (2015). A surviving intact branch stabilizes remaining axon architecture after injury as revealed by in vivo imaging in the mouse spinal cord. Neuron *86*, 947–954. https://doi.org/10.1016/j.neuron.2015.03.061.

39. Pang, J.J., Gao, F., and Wu, S.M. (2003). Light-evoked excitatory and inhibitory synaptic inputs to ON and OFF alpha ganglion cells in the mouse retina. J. Neurosci. *23*, 6063–6073.

40. Murphy, G.J., and Rieke, F. (2011). Electrical synaptic input to ganglion cells underlies differences in the output and absolute sensitivity of parallel retinal circuits. J. Neurosci. *31*, 12218–12228. https://doi.org/10.1523/JNEUROSCI.3241-11.2011.

41. Berson, D.M., Dunn, F.A., and Takao, M. (2002). Phototransduction by retinal ganglion cells that set the circadian clock. Science *295*, 1070–1073. https://doi.org/10.1126/science.1067262.

42. Guo, X., Zhou, J., Starr, C., Mohns, E.J., Li, Y., Chen, E.P., Yoon, Y., Kellner, C.P., Tanaka, K., Wang, H., et al. (2021). Preservation of vision after CaMKII-mediated protection of retinal ganglion cells. Cell *184*, 4299–4314.e12. https://doi.org/10.1016/j.cell.2021.06.031.

STAR★METHODS

KEY RESOURCES TABLE

REAGENT or RESOURCE	SOURCE	IDENTIFIER
Antibodies		
Guinea pig anti-Rbpms	Raygene	Cat# A008712
Rabbit anti-c-Fos	Cell Signaling	RRID: AB_2247211
Rabbit anti-CamKII (phospho T286)	Abcam	Cat# ab32678; RRID: AB_725893
Rabit anti-CaMKII	Abcam	Cat# ab52476; RRID:AB_868641
Rabbit anti-CREB (phosphor S133)	Abcam	Cat# ab32096; RRID:AB_731734
Rabbit anti-CART	Phoenix Pharmaceticals	Cat # H-003-62 RRID: AB_2313614
Guinea pig anti-Brn3a	Synaptic Systems	Cat #: 411 004 RRID: AB_2800538
Rabbit anti-Calbindin	Swant-Swiss Antibodies	Cat #: CB38a RRID: AB_2792808
Bacterial and virus strains		
AAV2-EF1a-FLEX-Twitch2b	Hope Center Viral Vector Core, This study	N/A
Chemicals, peptides, and recombinant proteins		
Tetrodotoxin (TTX)	Sigma	T8024
Strychinine	Sigma	S0532
Bicuculine	Sigma	14340
Atropine	Sigma	A0132
Phenylepherine	Sigma	P6126
EGTA, Tetra(acetoxymethyl Ester) (EGTA, AM)	ThermoFisher	E1219
Experimental models: Organisms/strains		
VGlut2-IRES-Cre	Jackson Labs	028863
Kcng4-Cre	Jackson Labs	029414
Opn4-Cre	Jackson Labs	021153
Recombinant DNA		
pAAV2-EF1a -FLEX-Twitch2b	This study	N/A
Software and algorithms		
ImageJ	NIH	RRID: SCR_003070
MATLAB	Mathworks	N/A

RESOURCE AVAILABILITY

Lead contact

Further information and requests for resources and reagents should be directed to and will be fulfilled by the lead contact, Philip R. Williams (prwillia@wustl.edu).

Materials availability

pAAV2-EF1a -FLEX-Twitch2b construct is available from the lead contact upon request.

Data and code availability

- The data reported in this paper will be shared by the lead contact upon request.
- This study did not generate any new code.
- Any additional information required to reanalyze the data reported in this paper is available from the lead contact upon request.

EXPERIMENTAL MODEL AND SUBJECT DETAILS

Animals

All experimental procedures were performed in accordance with animal protocols approved by the International Animal Care and Use Committee at Washington University in St. Louis Medical School and in compliance with the NIH Guide for the Care and Use of Laboratory Animals. Male and female mice were used dependent on litters and separated in cohorts of 3–5 siblings. For Cre dependent expression of virus in RGCs or subsets of RGCs, VGlut2-IRES-Cre (028863; Jackson Labs), KCNG4-Cre (029414; Jackson Labs) and Opn4-Cre (021153; Jackson Labs) mouse lines were obtained from Jackson Laboratories. Mice were aged approximately four weeks prior to viral injections and injuries were performed on mice at 6–8 weeks of age. VGlut2-Cre mice aged 8–12 weeks were used for non-crush experiments. Mice were housed in a barrier facility in Washington University School of Medicine with 12-h light/dark cycles at 21°C.

METHOD DETAILS

Intravitreal AAV injections

To measure cytoplasmic calcium levels, we used an FRET based ratiometric biosensor, Twitch2b, which uses a mCerulean 3 and cpVenus FRET pair with a troponin C minimal calcium binding motif (Kd = ~200nM). The Twitch2b calcium reporter sequence was obtained from a Twitch2b pcDNA3 plasmid (Addgene plasmid # 39531, RRID: Addgene_49531 [20]), and cloned into a Cre-dependent AAV expression construct using traditional cloning methods. This construct was packaged into AAV2 by The Hope Center Viral Vectors Core at Washington University in St. Louis. The titers of viral preparations ranged from 2×10^{12} to 1.0×10^{13} GC/mL as measured by qPCR. Virus was stored in 10 or 20μL aliquots in a −80°C freezer.

Mice were anesthetized by intraperitoneal injection of a ketamine and xylazine cocktail (KX) (10 mg/mL and 1 mg/mL respectively) in saline at a dose of 10 μL/g body weight. A pulled-glass micropipette was inserted near the peripheral retina behind the ora serrata and deliberately angled to avoid damage to the lens. Approximately 1 μL of vitreous humor was removed prior to viral injection. Virus aliquots were centrifuged for at least 30s prior to injection to remove air bubbles. Between 1.5 and 2 μL of AAV was injected intravitreally using a Hamilton syringe (80950, Hamilton). Any injections resulting in air within the vitreous or lens injury were not included in the dataset. An anti-bacterial ophthalmic ointment, Terramycin (Zoetis, NADA #8–763) was applied post-operatively to protect the cornea. All animals received subcutaneous Meloxicam (10 mg/mL) at a dose of 10 μL/g of body weight as a postoperative analgesic.

In vivo imaging of mouse retinal ganglion cells

Two-photon *in vivo* imaging of RGCs was carried out as recently described.[21] A Scientifica Hyperscope was used for *in vivo* image acquisition. This consists of a Mai Tai HP 100 fs pulsed laser (Spectrophysics), a pockels cell to modulate laser power, and a pair of glavo mirrors for beam steering. A 20 mm working distance objective (Mitutoyo, 20X air, 0.4 N.A., 378-824-5) was used for relay of the mouse lens and a motorized objective mount for z-stepping. A Chromoflex light collection system paired with GaAsP photo-multiplier tube (PMT) detectors (Scientifica) was used to acquire fluorescence emission signals. To visualize the emission signal from the Twitch-2b sensor, we used a filter cube consisting of a 505 long pass dichroic and 480/40 and 535/30 band-pass filter pairs to separate the cyan fluorescent protein (CFP) signal and yellow fluorescent protein (YFP) signal.

Mice were anesthetized with KX cocktail as described above and placed in an imaging head holder (SGM 4, Narishige) to keep stationary while imaging. The head of the mouse was secured with pins inserted into the ear canals and a bite bar to hold the maxillary incisors. A solution of 1% w/v atropine and 2.5% w/v phenylephrine hydrochloride in RO water was applied with an eye dropper to both eyes for pupil dilation, and animals were placed in the dark for 5–15 min prior to being put under the objective. Genteal-tears eye ointment (Alcon Inc.) was applied to both eyes and the head of the mouse was angled to align the iris with the light path. A #1.5 coverslip was placed in a compact filter holder (Thorlabs, DH1) and the holder was fixed to the microscope stage, allowing for the coverslip to be held perpendicular to the light path centered on the imaging area. Using LED epifluorescence light to visualize fluorescent cells, the head holder was adjusted to "flatten" the imaging area and reduce signal noise due to eye curvature. Most adjustments were made along the dorsal-ventral axis by rotating the mouse in the head holder. Altering the long angle or height of the head holder was needed to adjust the nasal-temporal axis.

Laser power measured out of the objective ranged from 20 to 45 mW and was limited to a maximum of 45 mW to prevent retina or cornea damage.[21] The Mai Tai pulsed laser was set at 850 nm to most effectively excite the Twitch-2b sensor.[17] ScanImage acquisition software (Vidreo Technologies) was used to obtain image stacks with an 8 μm z-stepping. Images (512 pixels × 512 pixels, 1 pixel ≅ $1\mu m^2$) were collected at 0.93 Hz with a 3-frame average. Retinas were scanned from the ganglion cell layer toward the inner nuclear layer to reduce photoreceptor activation. Other imaging settings like PMT voltage, bias voltage, and digital zoom were kept constant across all images.

Chronic time-lapse imaging

VGlut2-Cre, KNCG4-Cre, and OPN4-Cre mice were imaged as described above prior to injury (pre-image). Optimal regions of the retina were identified for chronic imaging, i.e., the region was relatively flat, had robust Twitch2b expression, and could be re-found quickly using vascular landmarks. All pre-images were obtained 100–300 μm away from the optic nerve head at the closest portion of the image. Either one, two, or three pre-images were obtained per retina, usually spanning the dorsal-temporal to ventral-temporal retina. For KCNG-Cre and OPN4-Cre chronic time lapses, three pre-images were obtained for all samples wherever possible.

Acute time-lapse imaging

VGlut2-Cre mice were imaged as described above prior to injury. After acquiring this pre-image, an injury was performed on the same eye that was pre-imaged. Animals were quickly put back into the head holder following injury and re-positioned to find the pre-imaged region. Subsequent images were acquired at 5-min intervals for at least 120 min. The mice were monitored every 30 min and occasionally an additional 0.05 mL of KX was injected intraperitonially as needed to keep the mouse asleep and still for at least 2 h. Genteal was reapplied at this time to both eyes as needed. It was important to consider laser power and potential damage to the retina with many images in succession, so we used the maximum laser power needed to acquire well-resolved images. This was between 20 and 30 mW for all samples and laser power was kept constant throughout the acute time-lapse. No deleterious effects were observed during the imaging session in crush or sham control samples and neither demonstrated laser-induced damage chronically. The region of interest was adjusted along with the z stack boundaries prior to each image acquisition as needed. A slight drift, especially in the z-direction, was common over the course of 2 h. For acute sham experiments, mice received the same protocol as described here except the final step of 'crushing' the optic nerve was not performed; the optic nerve was exposed and forceps were only placed around it. After the initial acute time-lapse, 3 of 4 mice from this cohort were tracked chronically as described above, allowing for determination of survival for RGCs that also had acute responses.

Injections and imaging

For pharmacological injection experiments (Figures 2G–2K), drugs were injected intravitreally with the same protocol as described above while the mouse was in the imaging head-holder. Four different groups of mice received injections of the following solutions: 1) A cocktail of inhibitory neurotransmitter receptors (3.33 mM bicuculline and 0.167 mM strychnine) in sterile saline. 2) Tetrototoxin (TTX) (1.25 mM) in sterile saline 3) Sterile saline control 4) No Injection control. Drug solutions were centrifuged for at least 30 s prior to injection to avoid bubbles. Animals were anesthetized with KX solution and placed in the imaging head holder for pre-injection images (pre-image). A pre-image was obtained as described above and animals were transferred to a nearby stereo-microscope where drug cocktail was injected in the vitreous space, all while still in the imaging head holder. Approximately 1 μL of solution was injected after removal of 0.5–1 μL of vitreous. A post-injection image was obtained 2–4 min after injection.

To reduce intracellular Ca^{2+}, we intravitreally injected the cell permeable calcium chelator ethyleneglycol-bis(β-aminoethyl)-N,N,N',N'-tetraacetoxymethyl ester (EGTA-AM, ThermoFisher, E1219). EGTA-AM was dissolved in a 1:1 solution of Dimethyl Sulfoxide (DMSO, Sigma Aldrich) and Phosphate Buffered Saline (PBS) at a concentration of 30 μM. Intravitreal injections were modified for EGTA-AM experiments by removing no vitreous, and injections of ~1-1.5uL were performed over a longer time (60 s) to prevent backflow of solution out of the eye. Control injections of vehicle only (DMSO:PBS, 1:1) were also performed. *In-vivo* imaging was performed as described above to obtain acute time-lapse images for up to 2 h after EGTA-AM injection. EGTA-AM injections were also performed during chronic longitudinal *in-vivo* imaging immediately after chronic survival tracking image acquisition to evaluate the effect of calcium removal on RGC survival.

Injury models

Bilateral optic nerve crush (ONC) injury was performed as previously described.[13] In brief, mice were anesthetized with KX as above and the optic nerve was exposed intraorbitally and crushed with fine forceps (Fine Science Tools, *Carbon* #5, No. 11251-10) for 10 s approximately 500 μm behind the optic disc. Anti-bacterial eye ointment was applied post-operatively to protect the cornea, and animals received subcutaneous Meloxicam (10 mg/mL) at a dose of 10 μL/g of body weight as a postoperative analgesic. Animal health was monitored for the first two days after ONC and every other day throughout the 14-day experiment. For acute time-lapse experiments, all samples took less than 3 min to re-find the region of interest, and given the few minutes required for image acquisition, the timing for the first image after ONC was 4.25 ± 0.48 min. For chronic time-lapse experiments, mice received a binocular ONC two days after their pre-image was taken. When evaluating the effect of EGTA-AM on survival, intravitreal injection was first performed immediately after ONC. Care was taken to avoid parts of the eye affected by the ONC surgery, where injections were performed at the nasal or dorsal portions of the eye rather than temporally.

Laser injury was performed directly within the retina using the 2-photon laser setup described above. After a pre-image was obtained, the desired injury location within the imaged region nearest to the optic head was identified. This area was navigated to while the nerve fiber layer was focused upon. The laser wavelength was shifted to 750 nm to reduce photobleaching, the laser power was set to 150 mW, and a 3 s point scan at 150 mW was performed for 3 s to induce a focused laser spot injury. The laser wavelength and power were returned to the previous *in vivo* imaging settings and the pre-imaged region was re-centered and re-focused. Timing for the first image after laser-burn injury was 2.25 ± 0.14 min and further acute time-lapse images were obtained as described above.

In vivo imaging analysis

Measuring ROIs: Intensity, variance, and normalization

Two-photon image analysis was performed using ImageJ software. Raw images were processed and made into two-channel (cpVenus (YFP), pseudo-colored magenta and mCerulean3 (CFP), pseudo-colored green) image stacks. Cell bodies were identified and manually labeled as individual elliptical regions of interest (ROIs) in their brightest and best resolved z section. Mean pixel values within each ROI for both CFP and YFP channels was measured in ImageJ and ratios were recorded and interpreted as physiological intracellular Ca^{2+} levels (R = YFP/CFP).

We further analyzed the measurements of each ROI by obtaining the variance of the YFP, CFP, and R values within each individual ROI. Using a custom MATLAB script, we obtained the average pixel intensity and standard deviation of the pixel intensity values for both the YFP and CFP channels as well as the total number of pixels within each ROI. We then calculated a standard error of the intensity in both channels for each ROI by dividing the standard deviation by the square root of the total pixel number. With this standard error, we obtained a high (TOP) and low (BOT) value at the 95% CI for both the YFP and CFP channels. We took the mean pixel intensity and added the standard deviation multiplied by a z-value of 1.645 (for 95% CI) to get the 'TOP' value and subtracted it to get the 'BOT' value. This allowed us to obtain a 'High Error' and 'Low Error' value by comparing the TOP and BOT 95% CI values for each channel with the following equations.

$$\text{High Error} = (\text{TOP})_{YFP}/(\text{BOT})_{CFP}$$
$$\text{Low Error} = (\text{BOT})_{YFP}/(\text{TOP})_{CFP}$$

These equations effectively gave us a 95% confidence interval for our ratio measurements which integrated the variance of pixel intensities for both the YFP and CFP channels. To filter cells using this error value, we calculated the 'Total Error' as 'High Error' minus 'Low Error' and normalized this value to each cells individual R values. This gave us a value we called the 'Percent Error'. We excluded highly variant RGCs with a 'Percent Error' higher than 60% and dim RGCs with a raw pixel intensity value (YFP + CFP) lower than 100, which primarily overlapped. For the survive vs. die and survival curve data (Figures 3B and 3C, respectively) no RGCs in the VGlut2-Cre samples were filtered out, <1% (1/197) of cells were filtered out of the KCNG-Cre samples (Figures 4B and 4C), and 19% (63/344) of cells originally quantified in the OPN4-Cre data were filtered out (Figures 4E and 4F). For the VGlut2 dynamic data (Figures 3E and 3F), 971 total ROIs were drawn on trackable cells throughout the chronic time-lapses. Out of these, 9% of cells (85/971) had higher than 60% percent error, while 15% of cells (146/971) were flagged qualitatively as non-reliable measurements. This included ROIs that appeared to have a high signal to noise or those that were not reliably tracked from one image to the next due to image quality or neurodegenerative changes in RGC topography. Out of the 85 total cells with high percent error, 95% of these cells (81/85) were also flagged qualitatively. Thus, cells that were neither flagged nor had higher than 60% error (85% of all ROIs, 825/971 cells) were included in the dynamic data.

Raw Twitch2b ratios were normalized across imaging setups by comparing two cohorts of VGlut2-cre experiments. All intensity values from the YFP and CFP channels were ranked in both cohorts and the 5^{th} and 95^{th} percentile values were identified and used to get a range for each channel, 'RangeYFP' and 'RangeCFP'. The ratio of RangeYFP in cohort 1 and 2 was used as a normalization factor for each channel, where ($\text{RangeYFP}_{[1]}/\text{RangeYFP}_{[2]}$) was multiplied by all YFP intensity values in cohort 2 and the same was done with $\text{RangeCFP}_{[1],[2]}$ with intensity values from the CFP channel. Cohort 1 was used as baseline and the distribution of all ratios from this cohort has a mean of 1.3526 and average YFP and CFP intensities of 985au and 588au, respectively (n = 22 retinas, cells = 1426). Prior to normalization, cohort 2 had a mean ratio of 1.029 and average YFP and CFP intensities of 482 a.u. and 485 a.u. (n = 23 retinas, RGCs = 1272), but after normalization the values in cohort 2 had a mean of 1.361 and an average YFP and CFP intensity of 1052 a.u. and 851 a.u. Normalized ratios from cohort 2 were used in acute ONC experiments (Figures 1B and 1C, n = 4 experimental, 3 sham), imaging and immunostaining experiments (Figure S1, n = 3; Figure 4E, n = 4.; Figure S2, n = 10) and control chronic time-lapse experiments (n = 4)). All other data is from cohort 1.

Chronic and acute time-lapse analysis

For both chronic and acute analysis, image stacks were processed by maximally projecting processed images to a single plane, combining the time series of max-projections into a t-stack multi-tiff, and aligning these images with the Linear Stack Alignment with SIFT plugin in ImageJ. ROIs were selected based on cells that could be tracked for all or most of the time-lapses. The mean number of trackable cells from a single retina was the following for each mouse line: VGlut2-Cre mice = 54 ± 5.8 cells, KCNG4-Cre mice = 15 ± 3.0 cells, and OPN4-Cre mice = 20 ± 3.0 cells (Mean ± SEM).

Laser injury experiments were analyzed depending on distance from the laser-burn location. The 'degeneration area' surrounding the laser-injury location was determined by evaluating which cells nearest the injury location did not atrophy over the first 20 min of imaging, which was different for each sample. This led to a concentric region 200–300 μm away from the laser injury location that marked the boundary for the degeneration area (Figure S2). Axon bundles and cells included in analysis all had axons that were directly on or adjacent (within 50 μm) to the laser injury location.

Chronic ONC image time-lapses varied in signal to noise due to a lesser dilation of the pupil, slight corneal opacity, and neurodegeneration throughout the ganglion cell layer causing increased axonal signal and decreased somatic signal. Additionally, not all cells were consistently within the image frame and were thus non-trackable at certain time points. Samples included in the 'Survival Curve' (Figure 3C) were time-lapses that were trackable in at least 6 out of 7 total images within the time-lapse, thus 5 out of 9 total samples included in the 'Survive vs. Die' (Figure 3B) analysis were used for 'Survival Curve' analysis (Figure 3C). Additionally, 3 out of 9 samples were suitable for 'Dynamic' analysis (Figures 3D–3F), which was more rigorous as cells needed to be both trackable and with enough signal to noise to obtain reliable Ca2+ measurements. The lack of a ROI expressing fluorescence at any imaging time point indicated cell death and was recorded as dead on the day of ROI loss. RGCs out of the imaging frame at one time point and found dead in the next observable time point were excluded from survival curve analyses.

Injection and imaging analysis

Image processing was performed as described above and pre-vs. post-injection images were aligned manually by eye. ROIs were selected based on if cells were both in-focus and in-frame in pre- and post-images. After that initial determination ROIs were drawn

on the pre-image blind to ratios in the post-image. The change in ratio from pre-image to post-image was quantified as the delta R/R_o, which was obtained by comparing the ratio of an ROI in the post-image, R_{post}, to the ROIs of the same cell in the pre image, R_{pre} ($R_{pre} = R_o$) with the following equation: $\Delta R/R_o = (R_{post} - R_{pre})/R_{pre}$.

With the assumption that the TTX injection causes a significant Ca^{2+} decrease in most RGCs with the capacity to decrease Ca^{2+}, we used the distribution of the post TTX injection experiments (Figure 2H) to define 'low' vs. 'high' Ca^{2+} levels. We quantified the mean and standard deviation of all cells after their eyes had been injected with TTX. Then, we calculated a threshold two standard deviations above this mean to differentiate between High Ca^{2+} and Low Ca^{2+} RGCs in the survival curves and survival dynamics analyses. It should also be noted that this threshold for high and low split the cells included in the VGlut2 survival curve (Figure 3C) approximately in half (124 high Ca^{2+}, 136 low Ca^{2+}.

Perfusions and Tissue preparation

All animals were given an intraperitoneal overdose injection of Tribromoethanol (Avertin, 500 mg/kg) (Sigma, T48402) and transcardiacally perfused with ice-cold Phosphate-Buffered Saline (PBS) followed by 100mL of 4% paraformaldehyde (Sigma) in PBS. Eyes were removed within 24–48 h of perfusion and retinas were dissected and preserved in PBS at 4°C.

Retinal wholemount immunostaining

After perfusion, whole retinas were kept in PBS at 4°C. Retinas sunk overnight in 30% sucrose in PBS at 4°C and freeze-thawed 3 times using dry ice and a glass slide. Samples were washed with PBS 3 times for 10 min and put in blocking solution (10% normal horse serum (Sigma, 158127) and 0.5% Triton X-100 (Sigma, 11332481001) in PBS) for 1–3 h at room temperature. Samples were placed in a solution of primary antibodies diluted in blocking solution on a shaker at 4°C for 5–7 days. Primary antibodies used were the following: Guinea pig anti-Rbpms (1:2000, Raygene A008712), Rabbit anti-*c*-Fos (1:500, Cell Signaling, 2250), Rabbit anti-pCamKII (1:100, Abcam, ab32678), Rabbit anti pan-CamKII (1:100, Abcam, ab52476) Rabbit anti-pCREB (1:100, Abcam, ab32678), and Rabbit anti-CART (1:1500, Phoenix Pharmaceuticals, H-003-62), Rabbit anti-Calbindin (1:2500, Swant, AB_2792808), and Guinea pig anti-Brn3a (1:500, AB_2800538). Retinas were washed with PBS 3 times for 10 min at room temperature. Secondary antibodies (Jackson ImmunoResearch) were diluted in blocking solution for 2–3 d at 4°C. Secondaries were raised in donkey against the primary antibodies host species, cross absorbed and conjugated to Alexa Fluor 568 or 647, and used at 1:500 dilution. After washing three times in PBS, whole retinas were mounted onto glass slides with Vectashield Antifade Mounting Medium (Vector Labs, H-1000-10).

For experiments stained with Rabbit anti-*c*-Fos, we first performed *in vivo* imaging of Twitch2b as described above for both eyes with two imaged regions per retina. Mice were then euthanized and enucleated 15 min after the last pre-image was acquired and retinas were drop-fixed in 4% paraformaldehyde in PBS for 1 h at room temperature. After staining with both cFos and Rbpms, confocal images were obtained. The same region of the retina used for *in vivo* imaging was identified in the retinal wholemounts. We quantified the intensity of cFos staining for RGCs that were also imaged *in vivo* by drawing ROIs around the Twitch2b confocal signal and measuring cFos channel intensity. This allowed for comparison of *in vivo* Twitch2b ratios to cFos levels post hoc. All Twitch2b positive cells were Rbpms positive. We then went to a nearby region on the wholemount completely outside of the *in vivo* imaged region to analyze the cFos intensity of non-imaged RGCs and drew ROIs around Twitch2b + Rbpms positive cells.

We used a similar protocol for experiments testing four other antibodies, Rabbit anti-pCamKII, Rabbit anti pan-CamKII, Rabbit anti-pCREB, and Rabbit anti-CART. We *in vivo* imaged both eyes with two image regions per retina. For the CART experiments, mice were immediately perfused after *in vivo* imaging. For the others, one group of mice was left as control and another received an optic nerve crush two days after the initial pre-image. Six days after the optic nerve crush we obtained a '6 day post crush' image (or 8 day post pre-image for control) of the same two imaged regions. Animals were then immediately perfused and retinas processed using the staining protocol described above.

RGC subtyping and immunostaining experiments were performed with KCNG-Cre mice to express Twitch2b in alpha RGCs specifically. *In-vivo* images were obtained as described above, retinas were dissected, mounted, and then stained for Brn3a and calbindin. The same region of the retina that was *in-vivo* imaged was identified to compare staining to *in-vivo* imaging results.

Confocal microscopy

An inverted laser scanning confocal microscope (Zeiss, Model 710) equipped with a 20× air objective (Zeiss 'Plan Apochromat', 0.8 NA, No10098) was used to acquire image stacks at a 2.0 μm z-spacing. A montage of a 4 X 4 tiled field of the retina surrounding the optic nerve head was obtained, the total region being 2100 μm × 2100 μm, and images were automatically stitched with the Zeiss Blue software. Using vascular and cellular landmarks, the *in vivo* imaged region was identified on the wholemount retina. No obvious signs of damage or degeneration were observed in the imaged region relative to the rest of the retina in both crushed and healthy samples for any of the experimental paradigms. Immunostained retinas were imaged for their respective antibodies as well as native Twitch2b fluorescence. For semiquantitative immunostaining, microscope settings were maintained consistent across samples. After image acquisition and identification of the *in vivo* imaged region, cells were confirmed as RGCs with Rbpms or Twitch2b and ROIs were drawn around the soma using this signal. The raw signal intensity was measured from the channel containing antibodies within these ROIs and normalized to the average intensity of each retina.

Electrophysiology

Mice were dark adapted for at least 2 h prior to euthanization with CO_2, decapitation, and enucleation. Retinas were then isolated under infrared illumination (>900 nM) in oxygenated mACSF containing (in mM) 125 NaCl, 2.5 KCl, 1 $MgCl_2$, 1.25 NaH_2PO_4, 2 $CaCl_2$, 20 glucose, 26 $NaHCO_3$ and 0.5 L-glutamine equilibrated with 95% O_2/5% CO_2 and flat mounted on a membrane disc (Anodisc, Whatman). Twitch2b positive RGCs were targeted at random under 2-photon microscopy (FV-1000 MPE, Olympus; Mai-Tai HP, SpectraPhysics) for cell-attached patch-clamp recordings while constantly superfused with warm (30°C–35°C) mACSF. Pipettes were filled with 160 mM NaCl, and voltage-clamped signals were amplified with a Multiclamp 700B amplifier (Molecular Devices) and filtered at 3 kHz (eightpole Bessel low-pass). Voltage signals were directly digitized via analog inputs on the 2-photon at the scan rate of the microscope (500 kHz) simultaneous to the Twitch2b FRET signal, which was excited at 850 nM and visualized using an emission filter set consisting of a 505 long pass dichroic mirror and 480/40 and 540/40 band pass filters to compute the YFP/CFP ratio. Dual electrophysiology and Twitch2b recordings were performed under resting (spontaneous) conditions. In some cases, solution containing 140 mM KCl was briefly puffed (PicospritzerII, Parker Hannifin) onto neuronal somata to induce periods of higher firing rates so as to obtain recordings across a wide dynamic range of firing rates and Twitch2b signal.

Electrophysiology analysis

For each recorded cell, electrophysiological traces were thresholded to spikes, and the RGC somata were segmented to compute the YFP/CFP Twitch2b FRET signal. An empirically measured ‘‘lag-time’’ of 750 ms between electrophysiological and imaging data was adjusted for by calculating the cross-correlation of their time vectors. Adjusting this lag-time between 0 and 5 s did not affect results. Firing rate and YFP/CFP signal were averaged into 5 s bins for each trace, and firing rate was then plotted as a function of YFP/CFP. Linear fits of this relationship were calculated for both individual cells and for the population of recorded cells. All analysis was done using custom MATLAB (Mathworks) scripts.

QUANTIFICATION AND STATISTICAL ANALYSIS

Statistical analyses were performed in Graphpad Prism 9. Details of statistical analyses including number of samples, what sample numbers represent, statistical tests used and value representations can be found in the Figure Legends and Results text. Unless otherwise indicated values are mean ± S.E.M. Significance was defined as a non-overlapping 95% confidence interval of samples means where calculated, or as a p value equal to or less than 0.05 for paired Student’s T test, rank sum tests or ANOVA.